Design of a Coreless Multi-Phase Electric Motor Using Magnetic Resonant Coupling

Besong John Ebot and Yasutaka Fujimoto

Department of Mathematics, Physics, Electrical Engineering and Computer Science, Yokohama National University, Yokohama 240-8501, Japan

With the emergence of electric vehicles and electric aircraft technologies, lightweight motors have become a requirement. Conventional motors are generally made up of coils, permanent magnets, heavy iron stators, and rotor cores. This article presents complete analytical modeling and design of a novel coreless multi-phase magnetic resonant motor (MMRM), conceptualized through the approach of magnetic resonance coupling. The removal of magnetic iron cores drastically reduces the weight of the resulting motor. The stator and rotor cores of the motor are made of reinforced plastic fibers and can be 3-D printed. Unrelated to the general operating principle of the existing conventional electric motors, resonant wireless power transfer (WPT) is the key feature of these motors. All the essential machine characteristics, such as self-inductance, mutual inductance, torque, and frequency domains, are fully developed. The mathematical modeling of the machine's physical phenomena is linked to its operation by simulation. This article shows the design concept and discusses the simulation procedure used to verify the developed analytical model through a finite-element analysis (FEA) from the established modeling topology equivalent to the proposed configuration motor model. Although the design is straightforward, an accurate analytical modeling and analysis are significant challenges to consider.

***Index Terms*—3-D printed, analytical model, multi-phase magnetic resonant motor (MMRM), mutual inductance, self-inductance, torque, wireless power transfer (WPT).**

I. Introduction

NEW developments in power electronics, especially converters and inverters, have used wireless power transfer (WPT) through magnetic resonance coupling to produce a wide range of applications. When applied to a transmitting and receiving coil in a WPT, magnetic resonance coupling will achieve a more significant distance between the coils, maintaining a high power transmission efficiency and considerable tolerance for the misalignment of the separated coils [1]–[6]. Magnetic resonance plays an important role in physics, because they provide a strong response to weak signals in weakly coupled coils. The concept of WPT using magnetic resonance coupling was first proposed in [1].

Different electric motors are built around a magnetic steel core. In most cases, the magnetic steel core accounts for more than 80% of the machine's weight and is used as a magnetic circuit to increase power density and torque [7]. To reduce the overall weight of the motor, new designs and models without the steel core have been proposed [8]–[13].

A coreless multi-phase magnetic resonance motor removes the iron core and its primary magnetic circuit, which account for most of the mass of the machine. This removal presents some practical advantages, especially in the case of saturation and iron loss elimination, good overload capability, low inertia and cogging torque, efficiency in high-speed operation, and a straightforward implementation [7], [10], [11]. In Fig. 1, a conceptual 3-D model of the multi-phase resonant magnetic motor is illustrated.

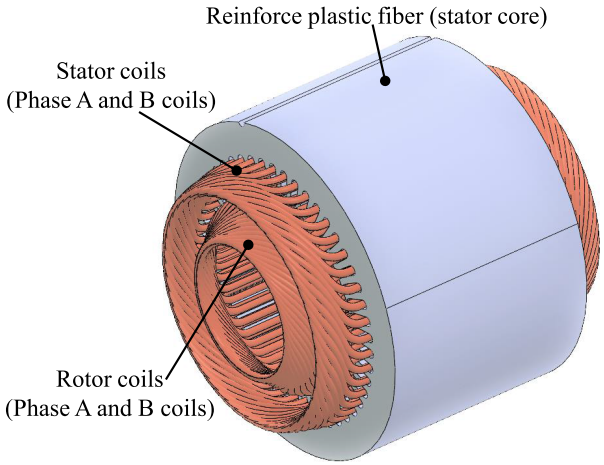

Fig. 1. 3-D model of a multi-phase resonant magnetic motor.

To make the motor coreless and air-cored, its stator and rotor cores are made of a reinforced plastic fiber that is a non-magnetic material. The air-gap length is essentially between stator and rotor phase windings. The effect of the design approach is that the magnetic load of the motor is drastically reduced, directly affecting the output torque of the motor. To improve the performance power rating, capacitors are introduced to the phase windings to offset the machine's inductive reactance and attain resonance under a specific slip to increase the electrical load at a given voltage. The capacitor that resonates with the leakage inductance compensates for the leakage inductance voltage drop and increases the current level with a constant rated voltage [14]. The torque improves

Manuscript received 30 December 2021; revised 17 May 2022 and 11 July 2022; accepted 17 July 2022. Date of publication 21 July 2022; date of current version 26 August 2022. Corresponding author: B. J. Ebot (e-mail: besongebot@yahoo.fr).

Color versions of one or more figures in this article are available at https://doi.org/10.1109/TMAG.2022.3193055.

Digital Object Identifier 10.1109/TMAG.2022.3193055

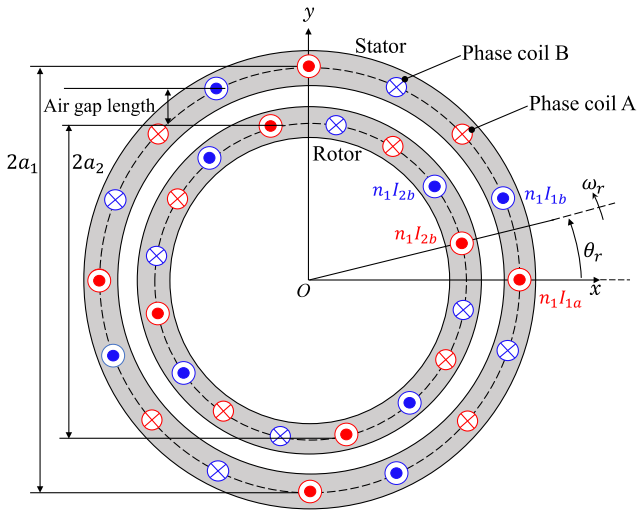

Fig. 2. Basic model of the MMRM.

at resonance, and the effective motor impedance reduces. The essential motivation behind the proposed coreless multi-phase magnetic resonant motor (MMRM) is the application of magnetic resonant coupling to electromechanical energy conversion systems in a consolidated approach. The air-gap length of such machines can be quite large. In addition, the air-cored non-magnetic structure avoids self-excitation with series capacitors, which would be a concern in iron-cored induction machines.

The proposed system is a two-phase coil machine with two primary windings at the stator and two secondary windings at the rotor. The multi-phase windings are tied to a multi-phase inverter. A benefit of having a multi-phase winding with capacitors in each phase tied to a multi-phase inverter is reduced winding harmonics. The multi-phase coils are represented with a red and blue radial pattern in Fig. 2, showing both the stator and the rotor of the motor. A total of four separate windings are used. The efficiency of the system fluctuates with its resonant frequency [8], [13].

This kind of a high-speed, coreless magnetic resonance induction motor is proposed in [8]–[13] and [15]–[22]. The equivalent circuits are the same for all the reported results model in these papers. It is important to note, however, that the structure proposed in [18]–[20] is a three-phase machine structure for both the stator and rotor coils that is different topologically to that presented in [8]–[13], which is a two-phase machine. However, the proposed machine characteristics, such as self- and mutual inductance, are not modeled, and the results in these papers are only based on a finite-element analysis (FEA) analysis with no corresponding established analytical model.

In [8], a similar concept is described for a linear-type MMRM. However, the frequency model used for the analysis was not fully developed. Ebot and Fujimoto [9]–[13] extended the model to a radial-type MMRM, and parameters of the machine are verified for different air-gap lengths reported in [10]. In [12], there is an attempt to develop a numerical model for this type of machine, and detail conditions for machine operations are also presented in this article.

A different method is applied in [21], where frequency splitting is used to create an excitation sequence in a multi-stator phase system. The generated torque is very small, and there is no analytical model of the motor parameters, such as torque.

In this article, advanced complete analytical mathematical models to design and analyze a novel multi-phase magnetic resonant electric motor are proposed. The torque generation is confirmed through the FEA of the equivalent analytical mathematical model configuration.

The proposed MMRM presented in this article falls under a new generation of air-core, magnetless, and coreless electric motors [6]. These types of electric motors have the following merits [9]–[13], [15]–[22].

1) Lighter in weight, since the stator and rotor cores are made of a non-magnetic-reinforced plastic fiber. Essentially, there is no core loss and flux saturation.
2) The magnitude and direction of the output torque can be controlled through the excitation frequency [15].
3) Regardless of the load conditions, the machine provides the inherent characteristics of unity power factor [18].
4) The rotor can extract power from the stator to power devices installed on the rotor side, regardless of the rotation speed of the motor.

In principle, the facilitation of the MMRM lightweight design is possible, because, in the high-frequency (HF) megahertz range, WPT does not necessarily need to use ferrite core material [20].

The rest of this article is organized as follows. Section II introduces the configuration and design layout related to the operation of the proposed motor, as well as a complete analytical mathematical model, in which the inductance, voltage, and torque equations are derived and extensively formulated. Section III describes the resonant frequency model of the entire motor circuit considering the influence of the rotor speed. In Section IV, the proposed theory of the motor is validated through FEA simulations, and the torque generation was confirmed. Section V discusses the results, and finally, Section VI summarizes this article.

II. Machine Configuration, Design, and Modeling

A. Theory of Machine Operation

An idealized cross-sectional model of the MMRM is shown in Fig. 2. The stator and rotor coils in the MMRM are a two-phase winding arrangement with the current direction, as shown in Fig. 2. The rotary actuation mechanism in this effort is similar to that in conventional induction motors, in which a current in the rotor coils needed to produce the torque is obtained from the magnetic field of the stator winding, otherwise, known as the field winding [7]. But, unlike in conventional induction machines, the current in the rotor winding is induced through magnetic resonant coupling technology within a resonant frequency. To achieve resonance, both the stator and rotor windings are connected to an added capacitance forming an LC coupled system.

The stator and rotor multi-phase winding systems of motor have a phase difference of 90°. To set up a rotating magnetic

field flux, sinusoidal voltage sources with the 90° phase difference are driven through the fixed stator winding mounted on the stator side of the proposed MMRM motor. This moving field flux induces currents in closed loops of wires winding mounted on the rotor. These currents set up magnetic fields around the windings and cause them to follow the main magnetic field as it rotates. The voltage frequency is close to the resonant frequency of the system. Compared with traditional induction motors, the air-gap length between the stator and rotor windings is larger.

B. Resonant Power Conversion Topologies

The electromechanical energy conversion in the motor is realized through a WPT resonant circuit topology. There are four main resonant topologies implemented in WPT, namely, series–series (SS), series–parallel (SP), parallel–series (PS), and parallel–parallel (PP) [23]. The first letter in the nomenclature indicates the type of compensation on the primary side, and the second shows the kind of resonance used on the secondary side.

The complexity for choosing a suitable topology is also discussed in [23]–[28]. These topologies, when implemented, determine the efficiency of the power transferred and delivered to the secondary side of the WPT systems, in which case the rotor winding of the motor. The four topologies are denoted as SS/SP/PP/PS for convenience. A benefit for utilizing the SS topology in the motor is applying high currents at low voltages and high speed.

C. Inductance Modeling

Considering the symmetrical configuration of the multi-phase windings in the motor, as shown in Fig. 2, single-phase simplified configuration, as shown in Fig. 3, is used for establishing the stator and rotor winding inductance models.

In a winding arrangement, as shown in Fig. 3, due to the current I of the conductor, there is an external magnetic field on the conductor. The magnetic field generated is modeled according to Ampere's law by considering an n number of turns in the winding

$$\boldsymbol{H}_0(x,y)=\begin{bmatrix}H_{0x}(x,y)\\ H_{0y}(x,y)\end{bmatrix}=\frac{nI}{2\pi(x^2+y^2)}\begin{bmatrix}-y\\ x\end{bmatrix} \tag{1}$$

where $\boldsymbol{H}_0(x,y)$ is the magnetic field vector at position (x,y) when the conductor is located at the origin. Since the wires that make up the stator windings of the motor are placed on the circumferential point of the stator core, the radial component of the magnetic field contributed by each stator winding is described as

$$\boldsymbol{H}_1(x,y)=\sum_{k=0}^{2p-1}(-1)^k\boldsymbol{H}_0\left(x-a_1\cos\frac{2\pi k}{p},\,y-a_1\sin\frac{2\pi k}{p}\right) \tag{2}$$

where p is the number of pole pairs of the machine, k is the winding constant used to reflect the coil pitch and distribution factors, and a_1 and a_2 are the radius from the origin O to the stator and rotor windings, respectively. The pole pair is calculated by the number of poles P_N as $p=(P_N/2)$. A vector

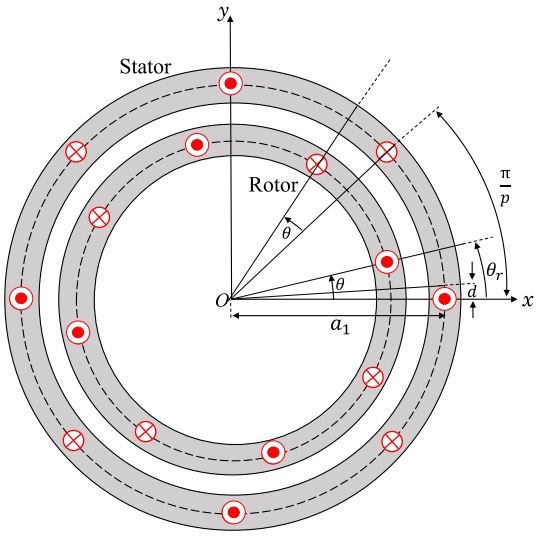

Fig. 3. Model for calculating self-inductance and mutual inductance.

plot of the magnetic field for the different pole pairs (for $p=1$, $p=3$, $p=6$, and $p=12$) using (2) of a typical MMRM is presented in [9].

From (2), the general expression of the self-flux linkage of the field winding within an arch path along the circumferential stator subspace in which the phase coils are arranged is given by

$$\Phi_L=\iint_{\mathcal{S}}\boldsymbol{H}_1\cdot\hat{u}_n\,ds \tag{3}$$

where $\hat{u}_n$ is a unit vector normal to ds, and $\mathcal{S}$ is a surface bounded by the coil windings.

The self-flux linkage can be resolved to Φ_{ex}, the field flux external to the coil winding, and Φ_{in}, the internal field flux in the coil windings. This is expressed as follows:

$$\Phi_L=\Phi_{\text{in}}+\Phi_{\text{ex}} \tag{4}$$

where Φ_{ex}, the external field flux is bounded in the region $[d/a_1,\pi/p-d/a_1]$, and Φ_{in}, the field flux inside the wire of the coil windings is bounded in the region $[0,d/a_1]$. The variable q is a spatial angle. Substituting (2) into (3) and integrating in the regions bounded by $\mathcal{S}$, the evaluation of the self-flux linkage computation is expressed as follows:

$$\begin{aligned}\Phi_{11}&=\mu_0 l_z n_1\int_0^{\frac{\pi}{p}}-[\cos q\quad \sin q]\boldsymbol{H}_1(a_1\cos q,a_1\sin q)a_1dq\\&=-\left[\frac{\mu_0 l_z n_1^2 I_1}{\pi}\int_0^{\frac{d}{a_1}}\left(\frac{q}{\frac{d}{a_1}}\right)\sum_{k=0}^{2p-1}\frac{(-1)^k}{2\tan\left(\frac{k\pi}{2p}-\frac{q}{2}\right)}dq\right.\\&\quad\left.+\frac{\mu_0 l_z n_1^2 I_1}{2\pi}\int_{\frac{d}{a_1}}^{\frac{\pi}{p}-\frac{d}{a_1}}\sum_{k=0}^{2p-1}\frac{(-1)^k}{2\tan\left(\frac{k\pi}{2p}-\frac{q}{2}\right)}dq\right]\\&=\underbrace{-\frac{\mu_0 l_z n_1^2 I_1}{\pi}\log\left[\tan\left(\frac{pd}{2a_1}\right)\right]}_{:=\Phi_{\text{ex}}}\\&\quad\underbrace{-\frac{\mu_0 l_z n_1^2 I_1}{\pi}\left(\frac{qa_1}{d}\right)\int_0^{\frac{d}{a_1}}\sum_{k=0}^{2p-1}\frac{(-1)^k}{2\tan\left(\frac{k\pi}{2p}-\frac{q}{2}\right)}dq}_{:=\Phi_{\text{in}}}\end{aligned} \tag{5}$$

TABLE I
COMPARING POLE PAIRS, WINDING WIRE RADIUS, AND INTERNAL AND EXTERNAL INDUCTANCES

Pole Pairs (p)	**Radius of wire** (d) mm	**External inductance** (L_{ex}) H	**Internal inductance** (L_{in}) H
1	1	1.1907×10^{-7}	2.2900×10^{-8}
	2	1.0318×10^{-7}	2.2901×10^{-8}
	3	5.5322×10^{-7}	2.9033×10^{-8}
	4	8.7283×10^{-8}	2.2904×10^{-8}
2	1	1.0318×10^{-7}	2.2901×10^{-8}
	2	8.7283×10^{-8}	2.2904×10^{-8}
	3	6.4653×10^{-7}	2.2908×10^{-8}
	4	7.1378×10^{-8}	2.2916×10^{-8}
3	1	9.3881×10^{-8}	2.9022×10^{-8}
	2	7.7981×10^{-8}	2.2909×10^{-8}
	3	7.0261×10^{-7}	2.2912×10^{-8}
	4	6.2061×10^{-8}	2.2935×10^{-8}
4	1	8.7283×10^{-8}	2.2904×10^{-8}
	2	7.1378×10^{-8}	2.2915×10^{-8}
	3	6.3408×10^{-7}	2.2923×10^{-8}
	4	5.5438×10^{-8}	2.2961×10^{-8}

where l_z is the stack length of the machine windings, d is the radius of the wire, and μ_0 is the permeability of free space.

From (5), the computation of the inductance of the stator winding can be derived. A good overview of modeling inductance is reported in [29]–[31]. Analogous machine configuration, analytical models of stator and rotor inductance are presented in [9]–[13], in which only the external field flux Φ_{ex} of the coil winding is considered.

As described in [31], when considering the fields corresponding to the external and internal fields of the coil winding, accurate analysis and computational modeling of inductance can be achieved. This extended inductance model will enable us to study other important characteristics of the motor, such as the skin effect and the influence of frequency on the current density distribution in the coil windings.

Therefore, from (5), the total inductance can be expressed as

$$L_i = L_{\text{ex}} + L_{\text{in}} \tag{6}$$

where L_{ex} is the external inductance, the part of the inductance associated with fields external to the coil windings, and L_{in} is the internal inductance, the part associated with the energy of the fields inside the wire windings, on a point d_i, such that $d_i < d$.

The stator winding self-inductance is, therefore, expressed as

$$L_1 = \underbrace{-\frac{\mu_0 l_z n_1^2}{\pi} \log\left[\tan\left(\frac{pd}{2a_1}\right)\right]}_{:=L_{\text{ex}}} \underbrace{-\frac{\mu_0 l_z n_1^2}{\pi}\left(\frac{qa_1}{d}\right)\int_0^{\frac{d}{a_1}} \sum_{k=0}^{2p-1} \frac{(-1)^k}{2\tan\left(\frac{k\pi}{2p} - \frac{q}{2}\right)} dq}_{:=L_{\text{in}}}. \tag{7}$$

The inductance model in (7) is a complete model, which is different from the one reported in [9]. As shown earlier, L_{ex} can be analytically computed for any number of pole pairs of the machine, whereas L_{in} becomes more complicated to compute, as the pole pairs increase.

From Table I, the following observations can be made about the internal inductance L_{in}.

1) As the wire size becomes smaller ($d \leq 1$ mm), compared with the external inductance L_{ex}, L_{in} will become insignificant. Therefore, L_{in} can be ignored in this case.
2) Larger wire sizes have more influence on L_{in}.
3) As the number of pole pairs p increases, the internal inductance L_{in} becomes significant and not negligible compared with the external inductance L_{ex}.
4) For all wire sizes and pole pairs, the external inductance L_{ex} is always higher than the internal inductance L_{in}.

A typical coil winding in the motor is made of wires of very small radius sizes (<1 mm). It can be assumed that uniform current density distribution exists throughout the wire radius. In such a case, L_{in} is dropped in the model.

The inductance analysis of the complete machine model is confined in two regions, viz., the stator windings and the rotor windings, and is expressed as

$$L_i = \begin{cases} L_1 = -\dfrac{\mu_0 l_z n_1^2}{\pi} \log\left[\tan\left(\dfrac{pd}{2a_1}\right)\right] \\ L_2 = -\dfrac{\mu_0 l_z n_2^2}{\pi} \log\left[\tan\left(\dfrac{pd}{2a_2}\right)\right] \end{cases} \tag{8}$$

where L_1 and L_2 are the self-inductance of the stator side and the rotor side, respectively.

The mutual flux linkage between the stator and rotor windings can be obtained along with the angular position of the

rotor over the boundary $[\theta, (\pi/p)+\theta]$, as follows:

$$\begin{aligned}\Phi_{12} &= \mu_0 l_z n_2 \int_{\theta}^{\frac{\pi}{p}+\theta} -[\cos q \quad \sin q]\boldsymbol{H}_1(a_2\cos q, a_2 \sin q)a_2 dq \\ &= -\frac{\mu_0 l_z n_1 n_2 I_1}{2\pi}\int_{\theta}^{\frac{\pi}{p}+\theta}\sum_{k=0}^{2p-1}\frac{(1)^k a_r \sin\left(\frac{k\pi}{p}-q\right)+1}{a_r^2-2a_r\cos\left(\frac{k\pi}{p}-q\right)+1}dq \\ &= -\frac{\mu_0 l_z n_1 n_2 I_1}{4\pi}\sum_{k=0}^{2p-1}(-1)^k \\ &\quad\times\left[\log\frac{a_r^2-2a_r\cos\left(\frac{k\pi}{p}-\theta\right)+1}{a_r^2-2a_r\cos\left(\frac{(k-1)\pi}{p}-\theta\right)+1}\right] \\ &= -\frac{\mu_0 l_z n_1 n_2 I_1}{2\pi}\log\frac{a_r^{2p}-2a_r^p\cos(p\theta)+1}{a_r^{2p}+2a_r^p\cos(p\theta)+1}. \end{aligned} \tag{9}$$

The mutual inductance between the stator and rotor windings is derived from (9) as follows:

$$M(\theta) = \frac{\Phi_{12}}{I_1} = -\frac{\mu_0 l_z n_1 n_2}{2\pi}\log\frac{a_r^{2p}-2a_r^p\cos(p\theta)+1}{a_r^{2p}+2a_r^p\cos(p\theta)+1}. \tag{10}$$

Further computation approximates (10) as follows:

$$M(\theta) \approx M_1\cos(p\theta)+M_3\cos(3p\theta) \tag{11}$$

$$M_1 = \frac{p}{\pi}\int_0^{\frac{2\pi}{p}} M(\theta)\cos(p\theta)d\theta = \begin{cases}\dfrac{2\mu_0 l_z n_1 n_2}{\pi a_r^p}, & (a_r > 1)\\ \dfrac{2\mu_0 l_z n_1 n_2}{\pi a_r^{-p}}, & (a_r < 1)\end{cases} \tag{12}$$

$$M_3 = \frac{p}{\pi}\int_0^{\frac{2\pi}{p}} M(\theta)\cos(3p\theta)d\theta = \begin{cases}\dfrac{2\mu_0 l_z n_1 n_2}{3\pi a_r^{3p}}, & (a_r > 1)\\ \dfrac{2\mu_0 l_z n_1 n_2}{3\pi a_r^{-3p}}, & (a_r < 1)\end{cases} \tag{13}$$

$$M(\theta) \approx \begin{cases}\dfrac{2\mu_0 l_z n_1 n_2}{\pi a_r^p}(\cos(p\theta)+\dfrac{1}{3a_r^{2p}}\cos(3p\theta)), & (a_r > 1)\\ \dfrac{2\mu_0 l_z n_1 n_2}{\pi a_r^{-p}}(\cos(p\theta)+\dfrac{1}{3a_r^{-2p}}\cos(3p\theta)), & (a_r < 1)\end{cases} \tag{14}$$

where $a_r = a_1/a_2$, and θ is the rotor electrical angle. In this article, $a_1 > a_2$ and $a_r > 1$. For an outrunner type of the motor, we will have $a_1 < a_2$, and hence, $a_r < 1$. Equation (14) expresses the interaction of the mutual inductance $M(\theta)$ with respect to the electrical angle θ because of the torque generated in the machine. Further analysis and traces of these variations are presented in [9].

D. Machine Circuit Analysis

The realization of the motor circuit is achieved by selecting a suitable resonance topology in the stator and rotor windings. The SS resonant topology minimizes the impedance on the stator side and maximizes the current amplitude [14], [27].

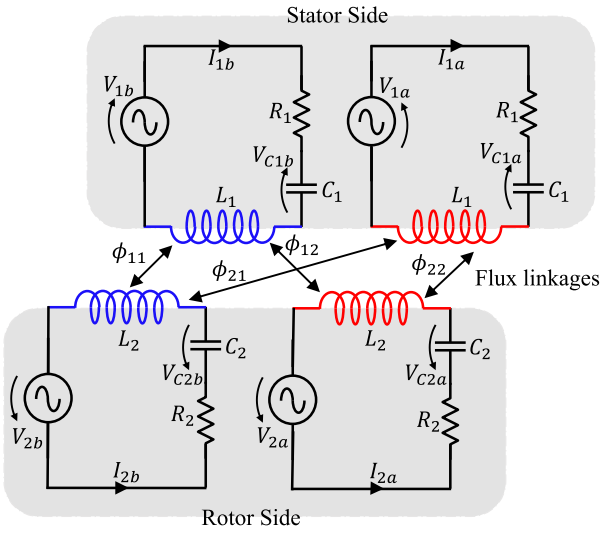

Fig. 4. Circuit model of MMRM.

The SS resonant topology also achieves good tolerance and better response to the fluctuations in the coupling coefficients of the windings. As shown in Fig. 4, the SS resonant topology is implemented in the machine. The equivalent circuit on the stator side and the rotor side is shown in Fig. 4. When the transmitting and receiving circuits are in resonance, the total impedance of the equivalent circuit will be minimized, resulting in a large current in the rotor winding.

The magnetic inductive resonant coupling between the stator and rotor windings varies per the rotation of the rotor. The inductance matrix of the windings $\boldsymbol{L}$ is expressed as

$$\boldsymbol{L} = \begin{bmatrix} L_1 & 0 & M_0\cos\theta & -M_0\sin\theta \\ 0 & L_1 & M_0\sin\theta & M_0\cos\theta \\ M_0\cos\theta & M_0\sin\theta & L_2 & 0 \\ -M_0\sin\theta & M_0\cos\theta & 0 & L_2 \end{bmatrix} \tag{15}$$

where M_0 is the optimal value of the mutual inductance between the stator and rotor windings. The stator and rotor winding inductances L_1 and L_2 are already defined in (8). When the air-gap diameter is $2a_2$, the pole pitch is defined as $\tau_p = 2\pi a_2/p$, and $\theta = (\pi/\tau_p)\theta_r$ is the electric angle of the rotor. The coupling coefficient between the transmitting stator winding and the receiving rotor winding changes according to the rotational movement. This is modeled in [9].

The voltage equation of the equivalent circuit is expressed as

$$\boldsymbol{V} = \boldsymbol{R}\boldsymbol{I} + \frac{d}{dt}(\boldsymbol{L}\boldsymbol{I}) + \boldsymbol{V}_C \tag{16}$$

$$\boldsymbol{I}_C = \boldsymbol{C}\frac{d\boldsymbol{V}_C}{dt} \tag{17}$$

where

$$\boldsymbol{V} = [V_{1a} \quad V_{1b} \quad V_{2a} \quad V_{2b}]^{\mathrm{T}} \tag{18}$$

$$\boldsymbol{I} = [I_{1a} \quad I_{1b} \quad I_{2a} \quad I_{2b}]^{\mathrm{T}} \tag{19}$$

$$\boldsymbol{R} = \mathrm{diag}(R_1, \quad R_1, \quad R_2, \quad R_2) \tag{20}$$

$$\boldsymbol{C} = \mathrm{diag}(C_1, \quad C_1, \quad C_2, \quad C_2) \tag{21}$$

$$\boldsymbol{V}_C = [V_{C1a} \quad V_{C1b} \quad V_{C2a} \quad V_{C2b}]^{\mathrm{T}} \tag{22}$$

and V_{1a}, V_{1b}, V_{2a}, and V_{1b} are the windings terminal voltages. I_{1a}, I_{1b}, I_{2a}, and I_{2b} are currents flowing in each circuits. R_1 and R_2 are resistances of the stator and rotor windings, C_1 and C_2 are parasitic capacitances of the stator and rotor windings, and V_{C1a}, V_{C1b}, V_{C2a}, and V_{C2b} are the voltage of these capacitors in their respective windings.

E. Torque Production

The generated torque is theoretically modeled and analyzed based on the magnetic energy product relative to the rotational movement in each sub-phase winding, as shown in the following:

$$T_e = \frac{\partial W}{\partial \theta_r} = \frac{d\theta}{d\theta_r}\frac{1}{2}\boldsymbol{I}^T\frac{\partial \boldsymbol{L}}{\partial \theta}\boldsymbol{I} \tag{23}$$

where θ_r is the mechanical angle describing the position of the rotor with respect to the stator.

Assuming that the currents flowing through the windings are sinusoidal and given by

$$I_{1a} = I_1 \sin(\omega_1 t) \tag{24}$$

$$I_{1b} = I_1 \sin\left(\omega_1 t - \frac{\pi}{2}\right) \tag{25}$$

$$I_{2a} = I_2 \sin(\omega_2 t - \delta) \tag{26}$$

$$I_{2b} = I_2 \sin\left(\omega_2 t - \delta - \frac{\pi}{2}\right) \tag{27}$$

where δ is a phase delay between the current in the stator and rotor windings, I_1 and ω_1 are the amplitude and the angular frequency of the current in the stator winding, and I_2 and ω_2 are those found on the rotor winding side.

The terminal voltage V_{1a}, V_{1b}, V_{2a}, and V_{2b} in each sub-phase winding is obtained substituting (24)–(27) into (15)–(22) as follows:

$$V_{1a} = R_1 I_1 \sin(\omega_1 t) + \left(\omega_1 L_1 - \frac{1}{\omega_1 C_1}\right) I_1 \cos(\omega_1 t) + (\omega_2 + \omega) M_0 I_2 \cos(\omega_2 t + \theta - \delta) \tag{28}$$

$$V_{1b} = -R_1 I_1 \cos(\omega_1 t) + \left(\omega_1 L_1 - \frac{1}{\omega_1 C_1}\right) I_1 \sin(\omega_1 t) + (\omega_2 + \omega) M_0 I_2 \sin(\omega_2 t + \theta - \delta) \tag{29}$$

$$V_{2a} = R_2 I_2 \sin(\omega_2 t - \delta) + \left(\omega_2 L_2 - \frac{1}{\omega_2 C_2}\right) I_2 \cos(\omega_2 t - \delta) + (\omega_1 - \omega) M_0 I_1 \cos(\omega_1 t - \theta) \tag{30}$$

$$V_{2b} = -R_2 I_2 \cos(\omega_2 t - \delta) + \left(\omega_2 L_2 - \frac{1}{\omega_2 C_2}\right) I_2 \sin(\omega_1 t - \delta) + (\omega_1 - \omega) M_0 I_1 \sin(\omega_1 t - \theta). \tag{31}$$

Therefore, the torque that is generated, as shown in (23), transforms into the form

$$T_e = \frac{\pi}{\tau_p} I_1 I_2 M_0 \sin((\omega_1 - \omega_2)t - \theta + \delta). \tag{32}$$

The rotor sub-phase windings are short-circuited as in conventional induction machines. However, in the MMRM, the equivalent circuit is closed to achieve short circuits by adding an external capacitance to each sub-phase winding. Hence, the condition for the rotor winding terminal voltages V_{2a} and V_{2b} in (30) and (31) to satisfy $V_{2a} = V_{2b} = 0$ is as follows:

$$\delta = -\tan^{-1}\frac{R_1}{\omega_2 L_2 - \frac{1}{\omega_2 C_2}} \tag{33}$$

$$I_2 = -\frac{\omega_2 M_0}{\sqrt{R_2^2 + \left(\omega_2 L_2 - \frac{1}{\omega_2 C_2}\right)^2}} I_1 \tag{34}$$

$$\omega_2 t = \omega_1 t - \theta \tag{35}$$

$$\omega_2 = \omega_1 - \omega. \tag{36}$$

In the expressions of δ, I_2, and ω_2 shown in (33), (34), and (36), these parameters are all obtained separately.

1) Current-Controlled Stator Power Source: The motor is current-controlled through the current that flows in the stator winding. Therefore, the generated torque follows the current in the stator phase windings. In this case, the torque is obtained substituting the solutions (37)–(40) into (28) and (29) and applying the voltage equation to the stator side of the machine as follows:

$$V_{1a} = I_1\sqrt{R_1^2 + \left(\omega_1 L_1 - \frac{1}{\omega_1 C_1}\right)^2}\cos(\omega_1 t + \gamma) + \omega_1 M_0 I_2 \cos(\omega_1 t - \delta) \tag{37}$$

$$V_{1b} = I_1\sqrt{R_1^2 + \left(\omega_1 L_1 - \frac{1}{\omega_1 C_1}\right)^2}\sin(\omega_1 t + \gamma) + \omega_1 M_0 I_2 \sin(\omega_1 t - \delta) \tag{38}$$

$$\gamma = -\tan^{-1}\frac{R_1}{\omega_1 L_1 - \frac{1}{\omega_1 C_1}}. \tag{39}$$

The torque controlled by the amplitude of stator current I_1 is derived substituting (33)–(36) into (32) as follows:

$$T_{e,i} = \frac{\pi}{\tau_p}\frac{(\omega_1 - \omega)M_0^2 R_2}{R_2^2 + \left(\omega_1 L_2 - \frac{1}{\omega_2 C_2}\right)^2} I_1^2. \tag{40}$$

The direction of the torque is controlled by the sign of the angular frequency of the stator currents ω_1.

2) Voltage-Controlled Stator Power Source: When the motor is voltage-controlled, the voltage of the sub-phase stator winding is considered as

$$V_{1a} = I_1 A \cos(\omega_1 + \beta) \tag{41}$$

$$V_{1b} = I_1 A \sin(\omega_1 + \beta) \tag{42}$$

where

$$A = \sqrt{R_1^2 + X_1^2 + \frac{\omega_1\omega_2 M_0^2\left(\omega_1\omega_2 M_0^2 + R_1 R_2 - X_1 X_2\right)}{R_2^2 + X_2^2}} \tag{43}$$

$$\beta = \tan^{-1}\frac{\omega_1\omega_2 M_0^2 R_2 + R_1\left(R_2^2 + X_2^2\right)}{\omega_1\omega_2 M_0^2 X_2 - X_1\left(R_2^2 + X_2^2\right)} \tag{44}$$

$$X_1 = \omega_1 L_1 - \frac{1}{\omega_1 C_1} \tag{45}$$

$$X_2 = \omega_2 L_2 - \frac{1}{\omega_2 C_2}. \tag{46}$$

Using (41)–(46) and substituting in (32), the voltage-controlled torque derived, as it scales quadratically with the amplitude of the stator voltage as follows:

$$T_{e,v} = \frac{\pi}{\tau_p}\frac{(\omega_1 - \omega)M_0^2 R_2}{D} V_1^2 \tag{47}$$

where

$$D = \left(R_1^2 + X_1^2\right)\left(R_2^2 + X_2^2\right) + \omega_1\omega_2 M_0^2\left(\omega_1\omega_2 M_0^2 + 2R_1R_2 - X_1X_2\right). \quad (48)$$

In (47), it is shown that the magnitude of the torque can be controlled by V_1 defined as $V_1 = (V_{1a}^2 + V_{1b}^2)^{1/2}$, the amplitude of the voltage source in the circuits of the stator windings. In addition, according to (40) and (47), the generated analytical torque is affected by the number of pole pairs and the size of the motor. This fluctuation can be found in the parameter π/τ_p.

All multi-phase stator and rotor windings are assumed to be tuned to a resonance condition. The further determination of these conditions will be discussed in Section III.

III. Selection of the Resonance Frequencies

The effectiveness of modeling the resonant frequency of the motor is to derive appropriate tuning options to evaluate the sufficient capacitance value of the capacitors that need to be added to the stator and rotor windings. The derivation of these frequencies is obtained by considering the influence of the rotor speed.

The initial condition assumed for simplification of resonance computation of the MMRM is $R_1 = R_2 = 0$. Using (43), the machine circuit impedance is set to zero under the condition that $A = 0$. As a result, the following hold:

$$\omega_1\omega_2 M_0^2 - \left(\omega_1 L_1 - \frac{1}{\omega_1 C_1}\right)\left(\omega_2 L_2 - \frac{1}{\omega_2 C_2}\right) = 0. \quad (49)$$

Equation (49) is effectively equivalent to $D = 0$ in (48) for the same condition $R_1 = R_2 = 0$. It is observed that the electric angle θ of the rotor is independent of this condition. However, the resonance frequency depends on the slip frequency $\omega_2(=\omega_1 - \omega)$, and the slip frequency also depends on the rotor frequency ω.

At resonance, the stator and rotor windings form a set of coupled resonators, so that the condition $L_1C_1 = L_2C_2$. This assumption makes it possible to further decompose (49), adding up the geometric mean $2(L_1L_2C_1C_2)^{1/2}$ and arithmetic mean $L_1C_1 + L_2C_2$ to zero. Consequently, we obtain four solutions to the equation in a complicated form. Taking a Taylor series expansion of the solution of the simplified equation with respect to ω_1 around $\omega = 0$ up to the first order evaluates to (50), as shown at the bottom of the page.

This solution presents an adequate model for the computation of the resonance frequencies of the machine in a generalized form. In (50), the stator and rotor inductances of the machine are both different, $L_1 \neq L_2$ and $C_1 \neq C_2$.

Suppose the motor parameters are designed, such that the self-inductance of the stator and rotor windings is the same ($L_1 = L_2$); then, for a series resonance in both the stator and the rotor coils, $C_1 = C_2$. Similar techniques are derived for a linear resonant motor in [8]. The reported results for the proposed linear resonant motor are typically only investigated and applied using a simple frequency model.

According to (50), the proposed MMRM has four resonance frequencies; two are in the negative frequency domain, and the other two are in the positive frequency domain. All resonant frequencies are shifted by half the frequency of the rotor.

A. Loses Due to HF

Significant losses in the motor can be accounted for by HF losses due to self-induced eddy currents that increase, as the frequency of the power source connected to the multi-phase stator winding increases. The resistance of the wire increases, as the frequency increases. The self-induced eddy currents are affected by L_{in}, the part of the inductance associated with the current density distribution in the winding. Changes in L_{in} are due to changing field flux Φ_{in} penetrating the coil. An increase in frequency decreases the current because of change in resistance.

The skin effect is difficult to model in the ideal model. Due to this phenomenon, as the frequency increases, current tends to concentrate in an annulus of the coils of skin depth δ. In a simple 2-D section cylindrical wire, $\delta = 1/(\pi\omega\mu_0\sigma)^{1/2}$, and its computation is straightforward in this case. This is not valid if we are to compute δ for a complete given pole pair of the MMRM. In that case, the computation becomes complex due to the complicated nature of modeling the current density because of the complexity of the field flux Φ_{in}, as shown in (5).

The skin effect is difficult to derive using our proposed ideal inductance model. Therefore, the consideration of the exact computation of the skin effect in the machine will be an open problem in our future works. Also, quasi-modeling these properties in resonant machines is reported in [32].

The analysis for theoretical model validation is performed at the frequency of 85 kHz. This is also the frequency of the power supply attached to the stator windings of the MMRM. Compared with conventional induction machines, this frequency is quite high and will increase frequency losses in the system that is associated with skin effect in the windings. The arrangement of the windings is a degree of freedom that allows for control losses. $D_i = 2d$ is the diameter of the wire in the coil winding. Another way to reduce HF losses is using copper Litz wires in both the stator and rotor windings to reduce the skin effect in the analysis. A high skin effect generated in the winding due to HF increases the impedance and affects the internal inductance L_{in} [30].

B. Quality Factor

Considering a single pole pair for the analysis, the quality factor is expressed as

$$Q_i = \frac{\omega_0 L_i}{R_i} \quad (51)$$

$$\omega_{1\text{res}} = \left\{ \frac{1}{\sqrt{(\sqrt{L_1L_2} - M_0)\sqrt{C_1C_2}}} + \frac{\omega}{2}, \quad -\frac{1}{\sqrt{(\sqrt{L_1L_2} - M_0)\sqrt{C_1C_2}}} + \frac{\omega}{2} \right.$$
$$\left. -\frac{1}{\sqrt{(\sqrt{L_1L_2} + M_0)\sqrt{C_1C_2}}} + \frac{\omega}{2}, \quad \frac{1}{\sqrt{(\sqrt{L_1L_2} + M_0)\sqrt{C_1C_2}}} + \frac{\omega}{2} \right\}. \quad (50)$$

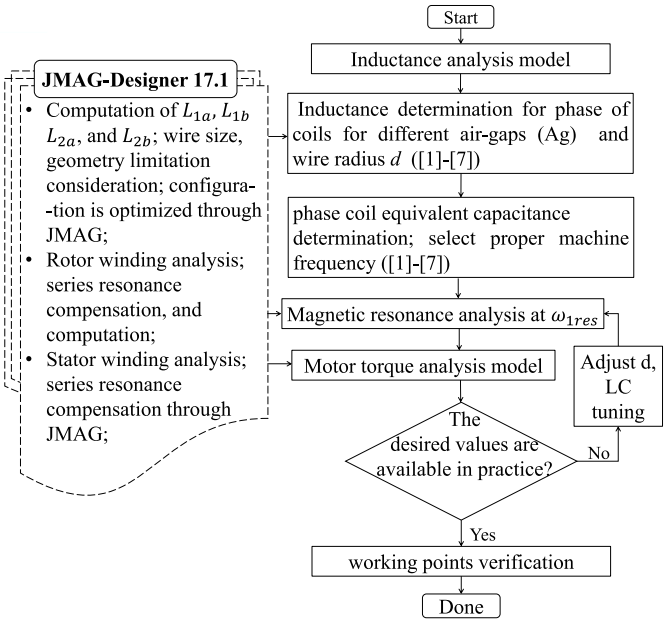

Fig. 5. FEA simulation procedure.

where $i = 1, 2$ denotes the stator and rotor windings, respectively. The total quality factor Q of the machine can be calculated from $Q = (Q_1 Q_2)^{1/2}$.

C. Efficiency

The total power transmission efficiency between the stator and rotor windings in the motor is affected mainly by the coupling of these coils and the quality factors of the interacting windings. This is fully derived from [23]. In general, the efficiency is calculated relative to a fixed load, which is usually connected to the receiving coil in the WPT system. This efficiency is defined as

$$\eta = \frac{(k_f Q_i)^2}{\left(1 + \left(\sqrt{1 + (k_f Q_i)^2}\right)^2\right.}. \tag{52}$$

Equation (52) is the efficiency of the machine's transmitter coil and receiver coil. The stator-coil–rotor-coil efficiency is calculated based on the coupling coefficients of the interacting windings and their respective quality coefficients.

Since there is no obvious load such as that in the traditional WPT system, the estimate of the actual power produced by the motor can be linked to this efficiency.

All analytical model derivations presented earlier were evaluated through complex algebraic manipulations using Wolfram-Mathematica 10.0.

IV. Analytical Validation Through 2-D FEA

The analytic models of all integral quantities (L_i, M_0, $T_{e,v}$, $T_{e,i}$, and $\omega_{1\text{res}}$) of the proposed MMRM developed earlier are validated through a 2-D FEA simulation.

The flowchart illustrating the procedure for the FEA simulation and methods of the validation is shown in Fig. 5. The quantities listed in the following are computed from FEA field solutions of the MMRM:

TABLE II
MMRM Parameters

Parameters	Values	Units
Outer diameter of Stator	200	[mm]
Stator winding placement (a_1)	90	[mm]
Outer diameter of Rotor	156	[mm]
Rotor winding placement (a_2)	68.5	[mm]
Stack length of coils	55	[mm]
Air-gap length	10	[mm]
Radius of wire	9	[mm]
Amplitude of voltage source	$V_1 = 100$	[V]
Frequency of power source	85	[kHz]
Resistance	$R_1 = R_2 = 3.29$	[mΩ]
Capacitance	$C_1 = C_2 = 1.2950$F	[μF]
Number of Turn of Coils	$N_1 = N_2 = 1$	NA

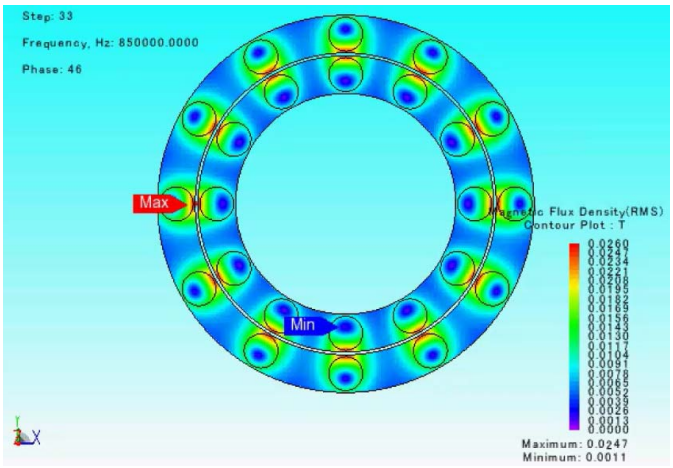

Fig. 6. Analytical and FEA computed inductance.

1) phase inductance in the rotor and stator phase windings L_{1a}, L_{1b}, L_{2a}, and L_{2b};
2) determination of the values of capacitance C_{1a}, C_{1b}, C_{2a}, and C_{2b} to be added phase coil windings;
3) phase currents I_{2a} and I_{2b} in the rotor phase windings;
4) torque $T_{e,v}$ or $T_{e,i}$.

The MMRM parameters used for the derivation of the FEA are shown in Table II.

The computation of the MMRM phase inductances L_{1a}, L_{1b}, L_{2a}, and L_{2b} is realized by the inductance analysis model in the FEA tool. For proper inductance validation with its corresponding analytical model expressed in (8), the geometry of the analysis model is equivalent to the proposed MMRM standard configuration shown in Fig. 2. Following this geometry, the phase windings of the stator are made of coils with the same wire size. This is the same in the rotor side of the MMRM. This is shown in Fig. 6. In the FEA analysis model, the stator and rotor cores are configured to be air-cored, viz., coreless. This coreless configuration reflects the reinforced plastic fibers shown in the 3-D model shown in Fig. 1.

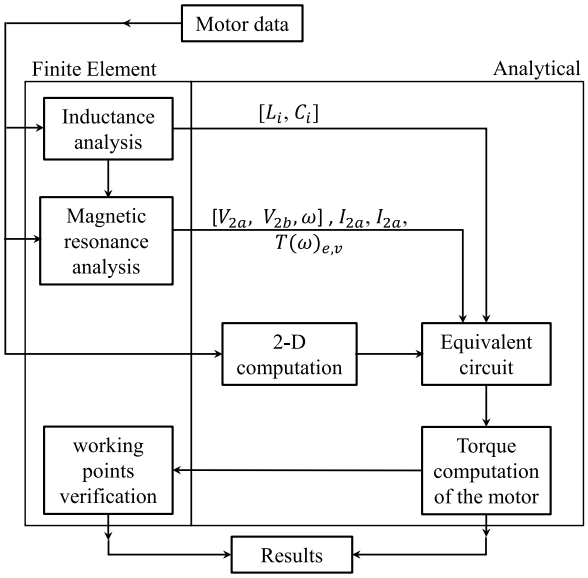

Fig. 7. Combined scheme of FEA–analytical procedure.

The frequency in which the inductance analysis is evaluated is $\omega_{1\text{res}}$, the same resonant frequency of the MMRM. In the frequency domain, only $\omega_{1\text{res}} \in \mathbb{R}_{++}$ is considered and used in the validation analysis.

The capacitance values C_{1a}, C_{1b}, C_{2a}, and C_{2b} are all calculated from determined inductance values, and the frequency model is expressed in (50). In the stator and rotor phase windings, typically, $C_{1a} = C_{1b}$ and $C_{2a} = C_{2b}$, respectively. These capacitors are also a source of losses in the MMRM [27], [31].

A magnetic field frequency analysis model is run to determine the torque and its fluctuations. The computed inductance, capacitance, and $\omega_{1\text{res}}$ stated earlier are used in this analysis. Other important integral values, such as the induced currents I_{2a} and I_{2b} in the rotor phase winding, can also be computed.

The abovementioned FEA simulation procedure is combined with the analysis model scheme. The combination scheme is shown in Fig. 7. This scheme serves as a reference through which the analytic models developed in this article are validated with simulations through FEA. Fig. 7 suggests that a parallel interaction between the schemes is used for validation, and feedback interaction between the methods is used for the optimization of the MMRM design. The reference scheme discrepancy determines the error rate in integral quantities verification.

V. FEA Simulations and Results

In this section, we validate the proposed multi-phase resonant motor's analytical model through FEA simulations. The proposed theoretical model of an MMRM through FEA can be validated for any given pole pair of the equivalent machine configuration. In this article, a three-pole pair ($p = 3$) equivalent model of MMRM is chosen to evaluate and conduct validation analysis. A wire of 9 mm diameter is used in the multi-phase winding of the machine, that is, in the stator and rotor multi-phase windings. The same pole pair number

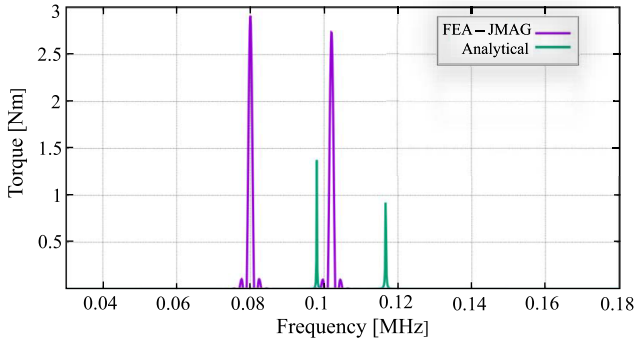

Fig. 8. FEA and analytical torque responses.

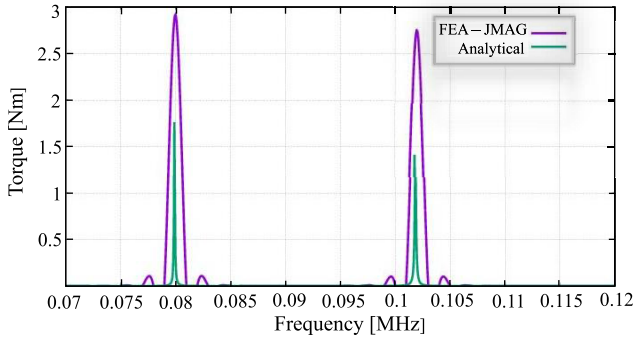

Fig. 9. Compensated LC FEA and analytical torque responses.

($p = 3$) equivalent model of MMRM is designed in the FEA tool.

The same geometric shape, as illustrated in Fig. 2, was used in the design. The three-pole pair MMRM design used for the FEA simulation is shown in Fig. 6. The condition for a uniform current distribution is assumed throughout the wire diameter. All simulation parameters are shown in Table II.

The torque responses of the three-pole pair model of the proposed MMRM are shown in Figs. 8 and 9. In these figures, results from the proposed MMRM model computed analytically and through FEA simulations of the frequency responses are shown. All FEA simulations were done using *JMAG-Designer-17.1*. The frequency used in the FEA simulations and analysis is 85 kHz. The analytically calculated value of the three-pole pair MMRM inductor considered in the proposed model is $L_{\text{analy}} = 9.18069 \times 10^{-8}$ H. The FEA field solution of the inductance is $L_{\text{FEA}} = 9.72706 \times 10^{-8}$ H. It has been shown in the previous studies [9], [10] that in the calculated winding inductance, the correlation between the calculated L_{analy} and FEA L_{FEA} is much closer for very small wire size. The current of 1 A is passed through the wire for inductance computation.

In the torque response shown in Fig. 8, the frequency of the voltage source $\omega_1 = 85$ kHz. The analytical torque response is lower than that of the FEA torque response.

This is seen in the differences in the amplitude of the torques. As shown in Table II, the values of the capacitance added to the multi-phase winding inductance are the same. Due to the differences in the inductance L_{analy} and L_{FEA}, there exists an offset in their respective bandwidths.

In Fig. 9, the analytic model of the MMRM and the FEA model are both LC compensated with respect to their

respective inductance, so that there has a common frequency response at 85 kHz. To do this, the number of turns n in the multi-phase windings is increased. In our validation process, n is increased to 30. This causes a slide in difference between the stator and rotor resulting inductance values. The added capacitance has different values. This allows the solution to operate at the same resonance instead of using the same capacitance value due to the difference in inductance slippage.

This improves the correlation of the analytical–FEA scheme and reduces the offset values between L_{analy} and L_{FEA}. The optimum torque for the FEA and analytical proposed models lies in the same frequency band. The amplitude of the torque response becomes much closer but that of the FEA model still remains higher.

The product of the torque and the speed of the rotor correspond to the mechanical power of the MMRM. One thing to note is that due to the design parameter, the inductance can be designed to be the same, but this affects the resistance of the windings. The resistances will be different due to different sizes of the stator and the rotor, $a_r > 1$. Since $a_1 > a_2$, it implies that the volume of the winding on the stator will be greater than that of the rotor.

The currents in the stator and rotor windings reach a steady state with the amplitude of around 58 A.

The optimal torque is 2.89 Nm, as shown in Figs. 8 and 9. The estimated weight of the machine design was 12 kg, and therefore, torque per kilogram of the machine is 0.241 Nm/kg. The output power density is 2.37 W/kg from analysis. The speed used in the analysis was 1000 rpm, which is low compared with other existing electric machines.

VI. Conclusion

In this article, a coreless MMRM is proposed. A complete analytical method is proposed to compute the inductance of the armature (stator) and excitation (rotor) windings in a radial gap coreless polyphase magnetic resonance motor. The proposed method is derived from the analytical solution of the Riemann surface winding in the motor and combined with the mirror image method to consider the stator and rotor core effects. As a first step, analytical formulas have been provided to calculate the mutual inductance between the motor stator and rotor windings, and these formulas have been verified against FEA simulations. The validated equation is then used to calculate the total torque, and the calculation result is again evaluated by comparison with FEA.

The precision of the inductance computation is made possible considering both the internal L_{in} and external inductances L_{ex}. It has been demonstrated that frequencies in the MHz domain will increase the winding impedance and affect the internal inductance L_{in}.

This extended inductance model can enable us to study essential machine behaviors, such as skin effect and influence on the current density distribution within the winding wire. In our studies, we developed a motor analysis model for a motor based on magnetic resonance coupling. The analysis methods used for the computation of the self and mutual inductances, coupling factors, and torques have all been formulated.

Since the MMRM operation frequency is very high compared with conventional motors, the chosen frequency must fall within the Industrial, Scientific and Medical reserved international bands (ISM) frequency band.

Acknowledgement

This work was supported in part by Grant-in-Aid for Scientific Research (KAKENHI) under Grant 21K18716.

References

[1] A. Kurs, A. Karalis, J. D. Joannopoulos, and M. Soljacic, "Wireless power transfer via strongly coupled magnetic resonance," *Science*, vol. 317, no. 5834, pp. 83–86, Jul. 2007.

[2] Z. Zhang, H. Pang, A. Georgiadis, and C. Cecati, "Wireless power transfer—An overview," *IEEE Trans. Ind. Electron.*, vol. 66, no. 2, pp. 1044–1058, Feb. 2019.

[3] S. Y. R. Hui, W. Zhong, and C. K. Lee, "A critical review of recent progress in mid-range wireless power transfer," *IEEE Trans. Power Electron.*, vol. 29, no. 9, pp. 4500–4511, Sep. 2014.

[4] A. P. Sample, D. T. Meyer, and J. R. Smith, "Analysis, experimental results, and range adaptation of magnetically coupled resonators for wireless power transfer," *IEEE Trans. Ind. Electron.*, vol. 58, no. 2, pp. 544–554, Feb. 2011.

[5] S.-H. Lee and R. D. Lorenz, "Development and validation of model for 95%-efficiency 220-W wireless power transfer over a 30-cm air GAP," *IEEE Trans. Appl. Ind.*, vol. 47, no. 6, pp. 2495–2504, Nov. 2011.

[6] J. Zhang, X. Yuan, C. Wang, and Y. He, "Comparative analysis of two-coil and three-coil structures for wireless power transfer," *IEEE Trans. Power Electron.*, vol. 32, no. 1, pp. 341–352, Jan. 2017.

[7] C. Liu, "Emerging electric machines and drives—An overview," *IEEE Trans. Energy Convers.*, vol. 33, no. 4, pp. 2270–2280, Dec. 2018.

[8] Y. Fujimoto, "Modeling and analysis of wireless electro-mechanical energy transfer and conversion using resonant inductive coupling," in *Proc. 41st Annu. Conf. IEEE Ind. Electron. Soc. (IECON)*, Nov. 2015, pp. 4905–4910.

[9] B. J. Ebot and Y. Fuiimoto, "A general framework for the analysis and design of a wireless resonant motor," in *Proc. IEEE Int. Electr. Mach. Drives Conf. (IEMDC)*, May 2019, pp. 1966–1970.

[10] B. J. Ebot and Y. Fujimoto, "A motor design based on wireless magnetic resonance coupling technology," in *Proc. IEEE Energy Convers. Congr. Exp. (ECCE)*, Oct. 2020, pp. 1140–1144.

[11] B. J. Ebot and Y. Fujimoto, "Design analysis for a novel wireless resonant actuator," in *Proc. IEEJ Int. Workshop Sens., Actuation, Motion Control, Optim. (SAMCON)*, Mar. 2018, pp. SS2–3.

[12] B. J. Ebot and Y. Fujimoto, "Design considerations for a novel wireless resonant actuator," in *Proc. IEEJ Int. Workshop Sens., Actuation, Motion Control Optim.*, Mar. 2017, pp. TT4–1.

[13] B. J. Ebot and Y. Fujimoto, "A simulation method for a motor design based on magnetic resonance coupling technology," in *Proc. 23rd Int. Conf. Elect. Mach. Syst. (ICEMS)*, Nov. 2020, pp. 369–373.

[14] M. Liu, H. Zhang, Y. Shao, J. Song, and C. Ma, "High-performance megahertz wireless power transfer: Topologies, modeling, and design," *IEEE Ind. Electron. Mag.*, vol. 15, no. 1, pp. 28–42, Mar. 2021.

[15] M. Boyvat, C. Hafner, and J. Leuthold, "Wireless control and selection of forces and torques–Towards wireless engines," *Sci. Rep.*, vol. 4, no. 1, Dec. 2014.

[16] K. Takishima and K. Sakai, "Starting characteristics of axial and radial type ultra-lightweight motors based on magnetic resonance coupling," *IEEJ J. Ind. Appl.*, vol. 8, no. 3, pp. 471–479, May 2019.

[17] K. Takishima and K. Sakai, "Design method for ultralightweight motor using magnetic resonance coupling and its characteristics," *IEEJ J. Ind. Appl.*, vol. 11, no. 1, pp. 76–87, Jan. 2022.

[18] K. Sakai and Y. Sugasawa, "Ultralightweight motor design using electromagnetic resonance coupling," in *Proc. IEEE Energy Convers. Congr. Exp. (ECCE)*, Sep. 2016, pp. 1–7.

[19] K. Sakai and K. Takijima, "Basic characteristics of an ultra-lightweight magnetic resonance coupling motor with various number of poles," in *Proc. IEEE Energy Convers. Congr. Exp. (ECCE)*, Sep. 2018, pp. 7342–7348.

[20] M. F. Iacchetti, R. P. Deodhar, A. C. Smith, and K. Mishima, "Modelling and operating characteristics of air-cored resonant induction machines," in *Proc. IEEE Energy Convers. Congr. Exp. (ECCE)*, Sep. 2018, pp. 6468–6475.

[21] M. Liu, K. W. Chan, J. Hu, Q. Lin, J. Liu, and W. Xu, "Design and realization of a coreless and magnetless electric motor using magnetic resonant coupling technology," *IEEE Trans. Energy Convers.*, vol. 34, no. 3, pp. 1200–1212, Sep. 2019.
[22] M. Vandeputte, L. Dupré, and G. Crevecoeur, "Quasi-static torque profile expressions for magnetic resonance-based remote actuation," *IEEE Trans. Energy Convers.*, vol. 34, no. 3, pp. 1255–1263, Sep. 2019.
[23] R. Jegadeesan and Y. X. Guo, "Topology selection and efficiency improvement of inductive power links," *IEEE Trans. Antennas Propag.*, vol. 60, no. 10, pp. 4846–4854, Oct. 2012.
[24] M. Fu, Z. Tang, and C. Ma, "Analysis and optimized design of compensation capacitors for a megahertz WPT system using full-bridge rectifier," *IEEE Trans. Ind. Informat.*, vol. 15, no. 1, pp. 95–104, Jan. 2019.
[25] T. Imura and Y. Hori, "Maximizing air GAP and efficiency of magnetic resonant coupling for wireless power transfer using equivalent circuit and Neumann formula," *IEEE Trans. Ind. Electron.*, vol. 58, no. 10, pp. 4746–4752, Oct. 2011.
[26] T. Yilmaz, N. Hasan, R. Zane, and Z. Pantic, "Multi-objective optimization of circular magnetic couplers for wireless power transfer applications," *IEEE Trans. Magn.*, vol. 53, no. 8, pp. 1–12, Aug. 2017.
[27] Z. Jin, M. F. Iacchetti, A. C. Smith, R. P. Deodhar, and K. Mishima, "Comparison of different capacitor tuning criteria in air-cored resonant induction machines," in *Proc. IEEE Energy Convers. Congr. Exp. (ECCE)*, Sep. 2019, pp. 3017–3024.
[28] N. Ha-Van and C. Seo, "Analytical and experimental investigations of omnidirectional wireless power transfer using a cubic transmitter," *IEEE Trans. Ind. Electron.*, vol. 65, no. 2, pp. 1358–1366, Feb. 2019.
[29] F. W. Grover, *Inductance Calculations: Working Formulas and Tables*. New York, NY, USA: Dover, 1962.
[30] C. R. Paul, *Inductance, Loop and Partial*. New York, NY, USA: Wiley, 2010.
[31] C. L. Holloway, E. F. Kuester, A. E. Ruehli, and G. Antonini, "Partial and internal inductance: Two of Clayton R. Paul's many passions," *IEEE Trans. Electromagn. Compat.*, vol. 55, no. 4, pp. 600–613, Apr. 2013.
[32] Z. Jin *et al.*, "Design optimization procedure of air-cored resonant induction machines," in *Proc. IEEE Energy Convers. Congr. Exp. (ECCE)*, Oct. 2021, pp. 4089–4096.

Besong John Ebot (Student Member, IEEE) received the B.S. degree in physics and computer science from the University of Buea, Buea, Cameroon, in 2009, the M.S. degree in industrial engineering from the École Nationale Supérieure Polytechnique Douala, University of Douala, Douala, Cameroon, in 2012, and the M.E. degree in electrical and computer engineering from Yokohama National University, Yokohama, Japan, in 2018, where he is currently pursuing the Ph.D. degree in electrical and computer engineering.

In 2016, he conducted an Overseas Summer Exchange Program, Department of Automation, Tsinghua University, Beijing, China. His research interests include electric machines design, wireless power transfer systems, electric vehicles, and new actuation technologies for mechatronics systems.

Prof. Ebot is a member of the IEEE Magnetics Society, Industrial Electronics, Power Electronic, and Industry Applications Societies.

Yasutaka Fujimoto (Senior Member, IEEE) received the B.E., M.E., and Ph.D. degrees from Yokohama National University, Yokohama, Japan, in 1993, 1995, and 1998, respectively, all in electrical and computer engineering.

In 1998, he joined the Department of Electrical Engineering, Keio University, Yokohama. Since 1999, he has been with the Department of Electrical and Computer Engineering, Yokohama National University, where he is currently a Professor. His research interests include actuators, robotics, manufacturing automation, and motion control.

Dr. Fujimoto is a Senior Member of the IEE of Japan and a member of the Robotics Society of Japan. He was a recipient of the IEEE/ASME TRANSACTION ON MECHATRONICS Best Paper Award in 2020. He is an Associate Editor of the IEEE TRANSACTIONS ON INDUSTRIAL ELECTRONICS and a Vice Chief of the *IEEJ Journal of Industry Applications*.